Desalination and Water Treatment
www.deswater.com

doi: 10.1080/19443994.2015.1049966

57 (2016) 11561–11571
May

Taylor & Francis
Taylor & Francis Group

Fluid structure and system dynamics in nanodevices for water desalination

Filippos Sofos*, Theodoros E. Karakasidis, Antonios Liakopoulos

Laboratory of Hydromechanics and Environmental Engineering, Department of Civil Engineering, School of Engineering, University of Thessaly, Volos, Greece, Tel. +30 24210 74329; email: fsofos@uth.gr (F. Sofos), Tel. +30 24210 74163; email: thkarak@uth.gr (T.E. Karakasidis), Tel. +30 24210 74111; email: aliakop@uth.gr (A. Liakopoulos)

Received 26 January 2015; Accepted 20 April 2015

ABSTRACT

Nanofluidic applications are currently being investigated in use for water treatment systems as a power efficient and effective means of removing undesirable substances from drinking or sea water. A detailed study of liquid nanoflows, in both simulation and experimental systems, is a prerequisite for establishing the theory and guiding the technological research and development toward this direction. In this work, we investigate the implications introduced when downsizing a flow system at the nanoscale with molecular dynamics simulations. It is shown that the presence of the walls, hydrophobic or hydrophilic that interacts strongly with fluid particles, is the main effect on flow properties at the nanoscale, although this effect is neglected by the continuum theory that describes flows at macroscopic scale. Furthermore, we estimate the Darcy–Weisbach friction factor for nanoflows of this type.

Keywords: Radial distribution function; Molecular dynamics; Desalination; Nanoflows; Friction factor; Energy loss

1. Introduction

Flows in nanotubes have been suggested for use in a significant number of applications including water desalination and purification. Recent advances suggest that many of the issues involving water quality could be resolved using nanoparticles, nanofiltration, or other products resulting from the development of nanotechnology [1,2]. Innovations in the development of novel technologies to desalinate water are among the most exciting and promising. Utilization of specific nanoparticles either embedded in membranes or embedded in other structural media can effectively, inexpensively, and rapidly render unusable water potable. Significantly high fluxes have been calculated for water flow through nanotubes [3–5]. Carbon nanotubes are gaining interest for water treatment systems, either as membranes or as electrode elements, and are close to pass from laboratory tests to commercialization [6,7].

Molecular dynamics simulations have been employed for studying, understanding, and predicting fluid behavior in atomic systems during the last decades [8,9]. Moreover, at the nanoscale, it is the most appropriate one since the assumption of continuous medium, conventionally employed in fluid dynamics breaks down [10]. A wide range of studies have

*Corresponding author.

Presented at the 12th International Conference on Protection and Restoration of the Environment (PRE XII) 29 June—3 July 2014, Skiathos Island, Greece

shown that as channel dimensions decrease, solid wall particles interact with the fluid and control its behavior, such as fluid atom positions, velocity, temperature, and transport properties such as diffusion coefficient, shear viscosity, and thermal conductivity [11–15].

Latest studies have shown that the boundary region between channel walls and the fluid presents particular interest since most fluid properties are affected within this region. The characterization of a surface as hydrophobic or hydrophilic leads to different behavior in this contact region [16]. Fluid atom localization near the walls, fluid velocity values, and viscosity [17–19] are among system properties that vary depending on the degree of wall wettability. Among fluid properties, the radial distribution function reveals fluid behavior since it represents the possibility of a fluid particle to exist in a specific channel position [8], but it also gives details about the structure of the fluid and the effect of the walls and the nanochannel dimensions on it.

Another approach for simulations is an hybrid continuum/molecular framework based on molecular dynamics. Researchers found that such an approach could enhance the applicability of nanofluidics in innovative technological applications [20]. In Asproulis et al. [21] such a multiscale approach is presented and the importance of accurate numerical modeling is pointed out, which, as in the majority of multiscale applications, depends on how clearly we define the transfer mechanisms between the molecular and the continuum regions [22] and how we save on the computational cost implied [23].

Another point that needs investigation in water applications is energy loss at the nanoscale. For example, the friction factor, f, although a macroscale quantity, is affected by fluid ordering at the nanoscale. Our simulations focus on providing a detailed investigation on how the structure of the fluid can affect fluid properties for several nanochannel widths and wall wettability degrees in a Poiseuille flow, establishing a theoretical basis so as to guide technological applications of nanofluidics for desalination and water purification.

The article is organized in the following way. In Section 2, the molecular model is described and computational details are given. In Section 3, calculated results on the radial distribution function, number density and velocity profiles, shear viscosity and the Darcy–Weisbach friction factor are presented and discussed in Section 4, focusing on their contribution on water desalination.

2. Computational details

2.1. Molecular dynamics parameters

The nanofluidic system modeled consists of two infinite plates with monoatomic particles flowing among them, and it is periodic along the x- and y- directions (Fig. 1). In this study, we employed nanochannels of increasing heights with values ranging from $h = 2.65\sigma$ to 50.1σ, where $\sigma = 0.3405$ nm. Details on channel dimensions and number of fluid and wall particles can be found in Table 1. The choice of model values is based on a previous study of transport properties of Poiseuille flow of argon [12] which have shown that the transport properties are significantly affected compared to the bulk for very small nanochannel width and they approach bulk values in the range of $h = 18$–50σ.

Atomic interactions are described by Lennard–Jones 12–6 type potential.

$$u^{\mathrm{LJ}}(r_{\mathrm{ij}}) = 4\varepsilon((\sigma/r_{\mathrm{ij}})^{12} - (\sigma/r_{\mathrm{ij}})^{6}) \quad (1)$$

where $\varepsilon/\mathrm{kB} = 119.8$ K, the fluid density is constant $\rho = 0.642\sigma^{-3}$, the cut-off radius is $r_c = 2.5\sigma$, and the atomic mass of fluid and wall particles is $m = 39.95$ a.u (equivalent to monoatomic argon fluid).

Wall atoms are kept around their original fcc lattice positions due to an elastic spring potential $u_{\mathrm{wall}}\left(\left|r(t) - r_{\mathrm{eq}}\right|\right) = \frac{1}{2}K\left(\left|r(t) - r_{\mathrm{eq}}\right|\right)^2$, where $r(t)$ is the position of an atom at time t, r_{eq} is its initial lattice

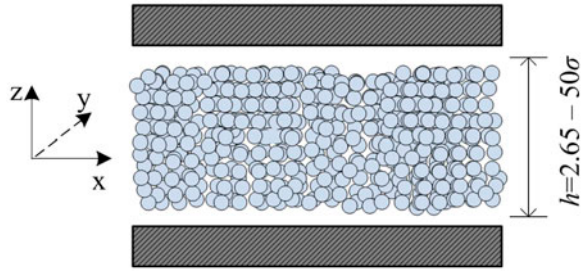

Fig. 1. Nanochannel model consisted of two infinite plates (equivalent of Poiseuille flow).

Table 1
Number of fluid atoms, N_f incorporated for each channel height h. Number of wall atoms is the same for every channel, $N_w = 288$

h/σ	2.65	4.42	7.9	18.58	50.1
N_f	192	320	576	1,344	3,648

position, and $K = 57.15\varepsilon/\sigma^2$ is the spring constant. This value satisfies the Lindemann criterion for melting and does not result in oscillating motion of wall particles being outside the regime that can be addressed in the molecular simulation time step.

An external driving force F_{ext} is applied along the x direction to every fluid particle during the simulation. The magnitude of the external applied force is selected in order to avoid nonlinear variations in fluid temperature induced by the flow [12]. The wall atoms absorb the increase in kinetic energy of the fluid atoms, and Nosé–Hoover thermostats at the thermal walls are employed in order to keep the system's temperature constant, $T = 1\varepsilon/\text{kB}$. We use two independent thermostats one for the upper wall and another for the lower wall in order to achieve better thermalization of the wall atoms.

A qualitative wall wettability parameter representing hydrophobic or hydrophilic behavior is $\varepsilon_{wall}/\varepsilon_{fluid}$ (from now on, $\varepsilon_w/\varepsilon_f$). This approach was also used in [16], where potential energy contours near the walls show that a large $\varepsilon_w/\varepsilon_f$ ratio (close to unity or more) leads in increased fluid atom presence near the walls (hydrophilic wall), while a small $\varepsilon_w/\varepsilon_f$ ratio (close to zero) leads in decreased fluid atom presence near the walls (hydrophobic wall). We investigate wall wettability effect for an $h = 18.58\sigma$ channel over the range $0.2 < \varepsilon_w/\varepsilon_f < 5.0$. However, there are also other methods to represent wall wettability. In [24], the ratio $\varepsilon_{wall-fluid}/\varepsilon_{fluid}$ is incorporated, which is analogous to our method.

The simulation step is $0.0046\ \sigma\sqrt{\frac{m}{\varepsilon}}$. In the beginning of a simulation, run fluid atoms are located on fcc sites. Atoms are assigned appropriate random initial velocities in order to reach the desired temperature. The system reaches equilibrium state after a run of 10^5 timesteps (NVE). Then, NEMD simulations are performed with duration of 10^6 timesteps.

2.2. Radial distribution function

The distribution of fluid atoms at the wall/fluid interface is investigated through the calculation of the radial distribution function.

$$g(r) = \frac{V}{N^2}\left\langle \sum_{i=1}^{N}\sum_{j\neq i}^{N}\delta(\mathbf{r}-\mathbf{r}_{ij})\right\rangle \tag{2}$$

where V is the spherical volume around the particle being investigated (see Fig. 2), N is the number of particles and the delta function, δ, represents a function which is nonzero in a small range of separations between the ith and the jth particle. The radial distribution function is an ensemble average over pairs of atoms and provides insight of the liquid structure [8].

In order to have a closer look on the distribution of fluid atoms, we can divide the channel region (for the $h = 18.58\sigma$ channel) in layers of width 1.325σ parallel to the nanochannel walls (at the z-direction), as shown schematically in Fig. 2, and calculate the local $g_{lay}(r)$ for each layer as:

$$g_{lay}(r) = \frac{V}{N_{lay}^2}\left\langle \sum_{i=1}^{N_{lay}}\sum_{j\neq i}^{N}\delta(\mathbf{r}-\mathbf{r}_{ij})\right\rangle \tag{3}$$

where N_{lay} is the number of fluid atoms in the channel layer investigated. The ith particle is located inside the layer investigated, while the jth particle can anywhere inside the radius of interaction.

Layer1 is the region between wall and fluid which is expected to provide the most interesting results. Wall effect is expected to reduce as distance from the wall increases, as this has been the case for transport properties [11] and many other static fluid properties [19].

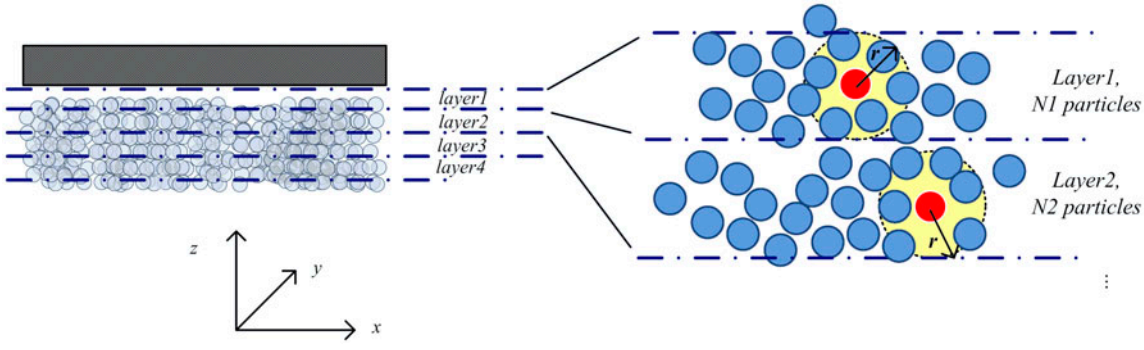

Fig. 2. Channel partitioning in layers. The local radial distribution function $g_{lay}(r)$ calculation is shown in each layer, according to Eq. (3).

2.3. Darcy–Weisbach friction factor

The relation giving the friction factor, according to Darcy, is as follows:

$$f = \frac{\left(\frac{\Delta p}{L}\right) D_h}{\frac{1}{2}\rho v^2} \tag{4}$$

where ρ is the mass density, Δp denotes the pressure drop along a channel segment of length L, v is the average fluid velocity at a cross section, and D_h is the hydraulic diameter. In simulation methods like MD, where periodic conditions are employed for the channel, the flow is not driven by a pressure difference Δp but by an external force F_{ext} applied to N fluid particles, so, consequently, $NF_{ext} \longleftrightarrow (\Delta p)A$, where A is the cross-section area. Moreover, if $\forbar{V}$ denotes the volume inside the channel and M the total mass between two successive channel cross sections, then

$$f = \frac{NF_{ext}\left(\frac{1}{A}\frac{V}{L}\right) D_h}{\frac{1}{2}Mv^2} \tag{5}$$

By substituting $\forbar{V} \approx AL$ and the particle mass $m = M/N$, Eq. (5) becomes:

$$f = \frac{F_{ext} D_h}{\frac{1}{2}mv^2} \tag{6}$$

The Reynolds number is defined as:

$$\mathrm{Re} = \frac{vD_h}{\nu} = \frac{vD_h}{\eta_s/\rho} \tag{7}$$

where ν is the kinematic viscosity, while η_s is the shear viscosity taken from the relations:

$$\eta_s = \frac{k_B T}{6\pi\sigma D_{ch}} (\text{Stokes} - \text{Einstein}) \tag{8}$$

$$\eta_s = \frac{k_B T}{4\pi\sigma D_{ch}} (\text{Sutherland}) \tag{9}$$

where D_{ch} is the channel average diffusion coefficient, taken from the Einstein's relation (see [12,13]).

$$D_{ch} = \lim_{t\to\infty} \frac{1}{6Nt} \left\langle \sum_{j=1}^{N} \left[\mathbf{r}_j(t) - \mathbf{r}_j(0)\right]^2 \right\rangle \tag{10}$$

The Sutherland relation (Eq. (9)) was found as a good estimate for channels of height $h > 20\sigma$, while the Stokes–Einstein (Eq. (8)) is a good estimate for $h < 20\sigma$, as seen in [13], where results obtained from this estimate were compared to results obtained from molecular dynamics simulations.

In a layer manner, local shear viscosity is as follows:

$$\eta_{s,lay} = \frac{k_B T}{6\pi\sigma D_{lay}} \tag{11}$$

with the local diffusion coefficient (calculated in channel layers), D_{lay}:

$$D_{lay} = \lim_{t\to\infty} \frac{1}{6N_{lay}t} \left\langle \sum_{j=1}^{N_{lay}} \left[\mathbf{r}_j(t) - \mathbf{r}_j(0)\right]^2 \right\rangle \tag{12}$$

3. Simulation results on fluid properties

3.1. Radial distribution function

Calculation of $g(r)$ has been performed in two ways: At first, we consider the walls and the fluid as averaged entities which interact with each other over the entire simulation duration. The radial distribution functions for wall/fluid and fluid/fluid interactions, for all channel cases investigated, are presented in Fig. 3((a)–(d)). We observe that the shape of $g(r)$ depends on whether we investigate the wall/fluid or the fluid/fluid distribution. The fluid/fluid distribution presents the first maximum around 0.9σ, a second maximum (of smaller magnitude) around 1.8σ, and stabilizes after the distance of 2σ, approaching a bulk-like behavior for nanochannels of $h > 18\sigma$.

As far as the wall/fluid distribution is concerned, i.e., the distribution of liquid atoms around the wall atoms, we point out some characteristic differences compared to the fluid/fluid distribution: (a) The first maximum lies on a larger distance (about 0.25σ) and its amplitude is smaller, (b) although it presents its first minimum at practically the same distance (1.3σ) as the fluid/fluid distribution, the second maxima and the bulk values are higher than that of the fluid/fluid distribution, especially for the channel cases of $h = 2.65$ and 4.42σ. The increase in bulk values for the two small channels may be attributed to the fact that $g(r)$ is calculated over a radius which is larger or comparable to the channel heights, and this probably introduces some noise.

The distribution of liquid atoms around a wall atom depends on the nanochannel height, h. As h

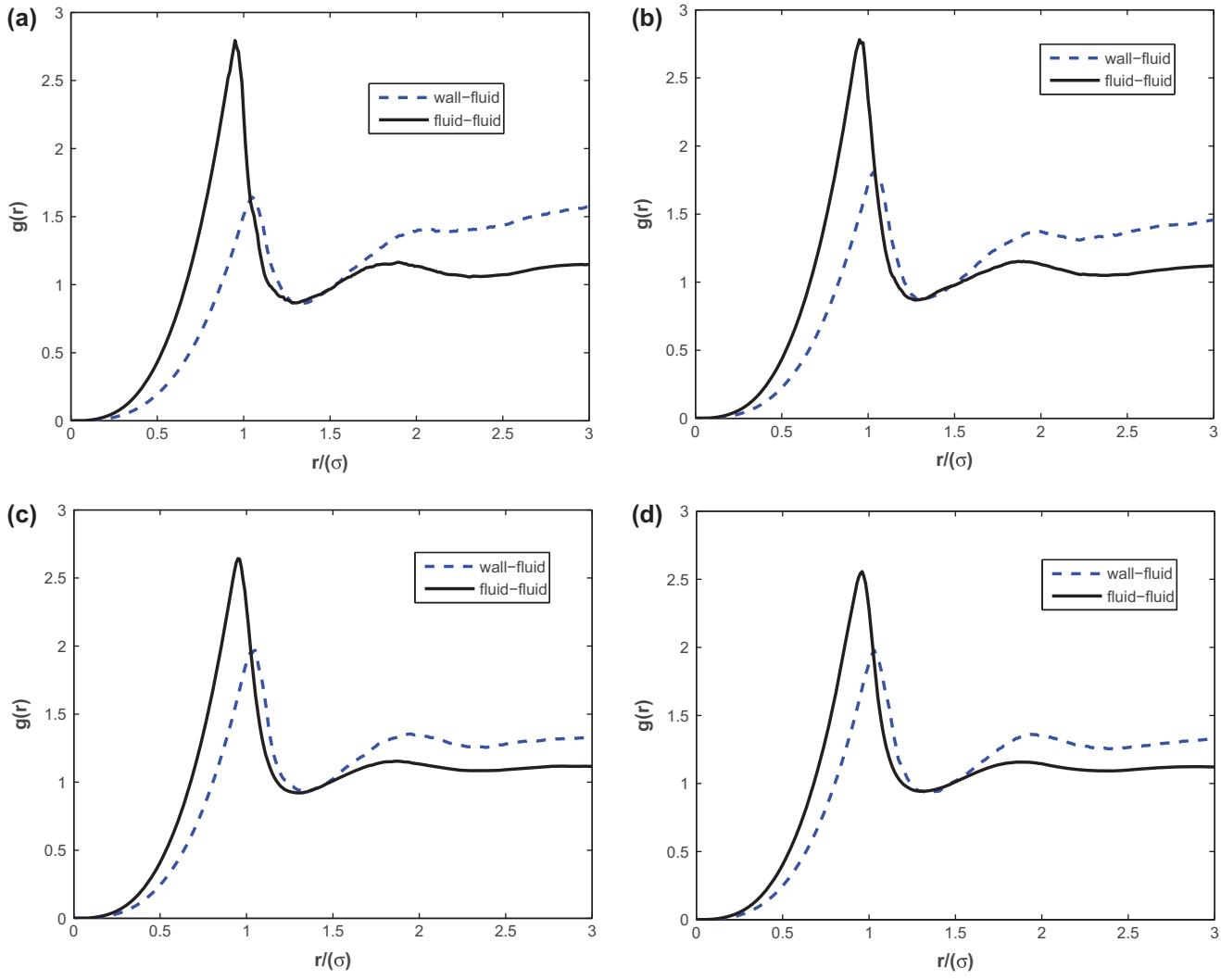

Fig. 3. Fluid/fluid and wall/fluid plot of $g(r)$ for channels of (a) $h = 2.65\sigma$, (b) $h = 4.42\sigma$ channel, (c) $h = 18.58\sigma$, and (d) $h = 50.1\sigma$.

increases, this distribution (as expressed by the magnitude of the first peak appeared) also increases, as one can see by comparing Fig. 3((a)–(b)) to Fig. 3((c)–(d)). This is consistent with number density results observed in molecular dynamics simulation [9] where, for small nanochannels, increased layering is observed, along with very low density of fluid atoms close to the wall and increased presence of fluid atoms at various regions in the inner region of the nanochannel, resulting in an increased oscillatory behavior of the density. However, this effect reduces significantly as the width of the nanochannel increases and especially above $h = 18\sigma$ while it is more pronounced for small nanochannels. This is attributed to the fact that the wall atoms interact with the fluid over a wide range of 2.5σ (the potential cut-off of the LJ potential), thus, modifying significantly the structure and properties of the fluid when the nanochannel height is comparable to 2.5σ.

By altering wall/fluid interaction ratio $\varepsilon_w/\varepsilon_f$ from 0.2 to 5.0, the behavior of channel walls change from hydrophobic to hydrophilic. It is of great interest to shed light on fluid behavior near the channel wall, since wall wettability influences mainly fluid properties near the walls [9]. Fig. 4(a) proves this local hypothesis, as for an $h = 18.58\sigma$ channel, we get almost similar diagrams for $g(r)$ for every $\varepsilon_w/\varepsilon_f$ studied, both for fluid/fluid and wall/fluid interactions, resembling the behavior of Fig. 3(c).

However, fluid behavior changes significantly if we take a closer investigation on the channel layer adjacent to the wall and calculate $g_{lay}(r)$, keeping in

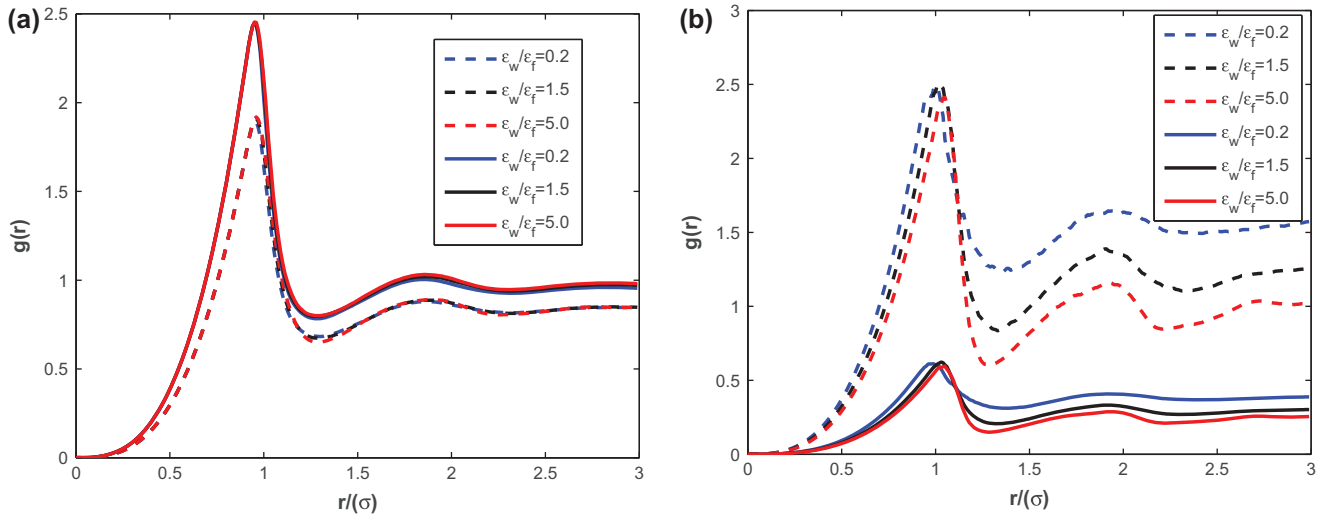

Fig. 4. Radial distribution function $g(r)$ for hydrophobic/hydrophilic walls in a channel of $h = 18.58\sigma$. (a) for the whole channel and (b) for local values at layer1. Continuous lines are for fluid/fluid distribution and dotted lines for wall/fluid distribution.

mind that the small bin size might introduce some noise on the results. Fig. 4(b) shows, at first, that now wall/fluid distribution is greater than fluid/fluid distributions for every wall wettability case studied here. This is expected since wall interaction is strong in this region and decreases as we move away from the wall. The hydrophobic wall ($\varepsilon_w/\varepsilon_f$ =0.2) seems to locate the distribution closer to the wall, compared to $\varepsilon_w/\varepsilon_f = 1.5$ and, at the hydrophilic wall ($\varepsilon_w/\varepsilon_f = 5.0$), we observe that $g(r)$ diagram is shifted to the right, even more far from the walls. Moreover, we observe that the distribution function for the strongly hydrophilic wall ($\varepsilon_w/\varepsilon_f = 5.0$) presents strong ordering, with sharp minima and maxima until it stabilizes to channel bulk, while, for the hydrophobic channel, radial distribution function decreases to channel bulk value after only one small peak at about 1.75σ.

3.2. Number density profiles

In order to compute the number density profile, the channel is divided into $n = 40$ bins along the z-direction, each one of volume $L_x \times L_y \times (h/n)$. The instantaneous fluid number density is expressed as

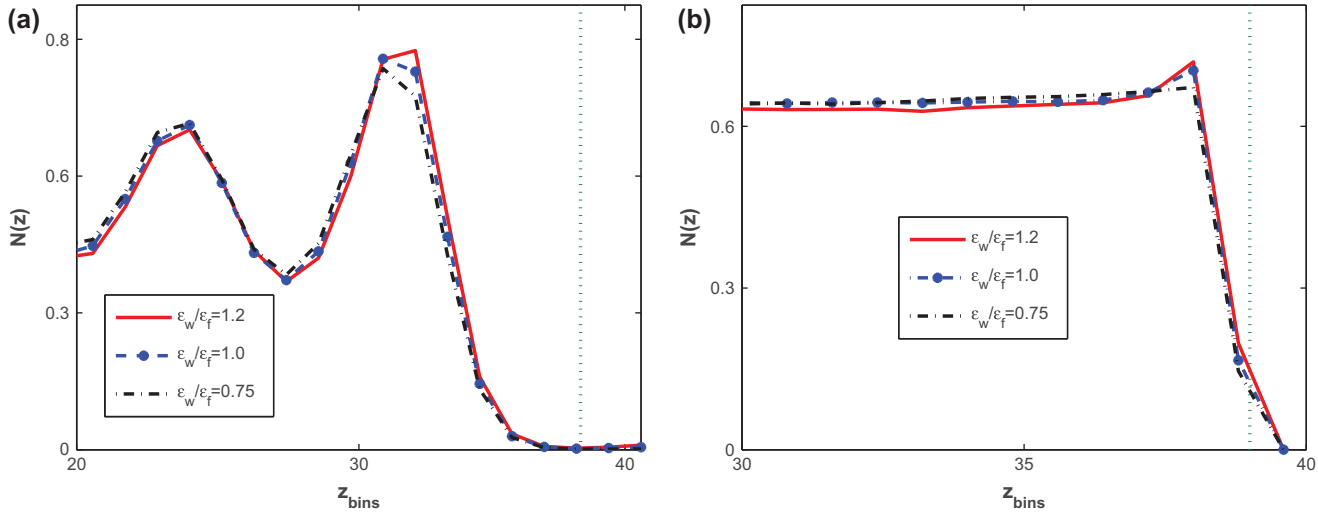

Fig. 5. Number density profiles for various wall wettability ratios and channels of height (a) $h = 4.42\sigma$ and (b) $h = 50.1\sigma$. Profiles are symmetric to the channel centerline and shown only in a region close to the wall. Dotted lines indicate the wall limit.

the number of particles located in each bin at a specific time step. This number is averaged over the total simulation time and a time-averaged value for each bin is extracted. Fig. 5(a) depicts number density profiles for an $h = 4.42\sigma$ channel, with three different $\varepsilon_w/\varepsilon_f$ values. At this channel size, wall/fluid interaction is strong and two fluid peaks appear in each channel half, denoting strong fluid inhomogeneity. The positions of the peaks in number density are equidistant, at about 0.9σ, from each other. A hydrophilic wall ($\varepsilon_w/\varepsilon_f = 1.2$) attracts fluid atoms to the wall, and stronger ordering is observed, as the number density peak adjacent to the wall has greater maxima compared to $\varepsilon_w/\varepsilon_f = 1.0$ and even greater compared to $\varepsilon_w/\varepsilon_f = 0.75$.

Fluid ordering in an $h = 50.1\sigma$ nanochannel (Fig. 5(b)) seems to be significantly decreased compared to $h = 4.42\sigma$ nanochannel. Number density profiles present inhomogeneity only in a small region adjacent to the walls and remain practically constant across the channel. However, near the walls, wall wettability is of importance, as the trend of increased fluid ordering appears past an hydrophilic wall and, on the other hand, decreased fluid ordering past an hydrophobic wall.

3.3. Velocity profiles

Calculations for velocity values are performed in 40 bins, as in the case of number density profiles described in Section 3.2. To extract the velocity profiles for a flat-wall channel, average velocity is computed at each bin for each time step and all these values are time-averaged. Results are depicted shown in Fig. 6((a)–(b)). Fig. 6(a) presents the effect of the channel width, under the same flow conditions. There is a clear increase in velocity values across the channel as system dimensions increase, under the same flow conditions. The amount of energy induced to the flow system from the application of the external force is increasing as h increases, and, as a result, we obtain large velocity values (e.g. for $h = 50.1\sigma$), which, can be fitted in a second-order polynomial function. On the other hand, when h is small (around 2–3σ), velocity values are very low and cannot be fitted to a second order polynomial function, and this is evidence of creeping flow. As far as wall wettability is concerned (Fig. 6(b)), we observe that a highly hydrophobic wall ($\varepsilon_w/\varepsilon_f = 0.2$) leads in increased velocity values across the channel, compared to values obtained from flow between highly hydrophobic walls ($\varepsilon_w/\varepsilon_f = 5.0$). We attribute this behavior to fluid ordering, as explained in the Section 3.1. As the channel wall becomes hydrophilic, stronger ordering is applied to fluid particles near the wall, reducing their mobility and, consequently, their velocity values.

From the velocity profiles presented in Fig. 6, we extract the average fluid velocity v to be used in Eqs. (6 and 7).

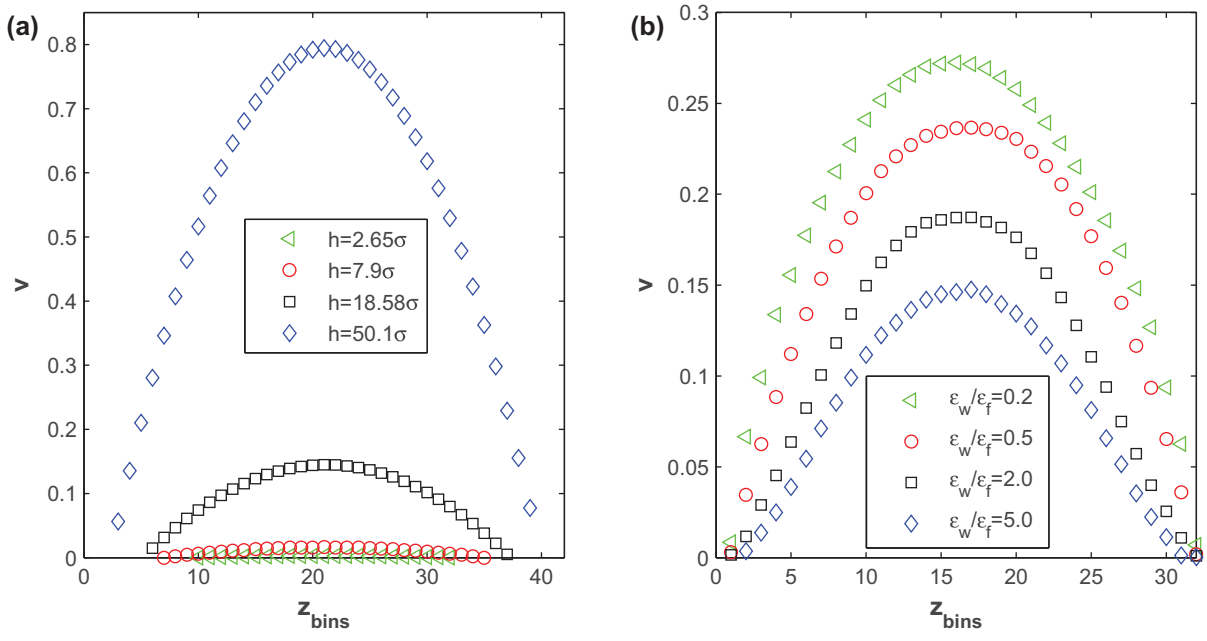

Fig. 6. Velocity profiles, with values shown in reduced LJ units $\sqrt{\frac{\varepsilon}{m}}$. Effect of (a) channel width, where $2.65\sigma < h < 50.1\sigma$. The horizontal axis refers to the channel height and is shown normalized, divided into 40 bins (z_{bins}) for each channel case. Simulation conditions are $F_{ext} = 0.0037\ \varepsilon/\sigma$ and $\varepsilon_w/\varepsilon f = 1$ and (b) wall wettability ratio, for the $h = 18.58\sigma$ case and $F_{ext} = 0.0074\ \varepsilon/\sigma$.

3.4. Shear viscosity

Fig. 7 displays shear viscosity values over each flow parameter investigated. There is a monotonic decrease for shear viscosity as the channel width increases toward the bulk value (Fig. 7(a)). The macroscale assumption of constant shear viscosity cannot be applied at the atomic scale; however, as channel dimensions approach 10–15σ, shear viscosity retains its bulk value. Fig. 7(b) reveals a monotonic increase in shear viscosity past a wall with increased hydrophilicity. We attribute this behavior to the fact that the radial distribution function revealed increased fluid atom presence near the hydrophilic wall (Fig. 4(b)). On the other hand, hydrophobic walls present smaller shear viscosity values, which is in agreement with slip length calculations in the literature, where a viscosity layer adjacent to the wall exists and correlates with slippage over a hydrophobic surface.

3.5. Reynolds number

Flows, at the nanoscale, are characterized by small Reynolds numbers due to system dimensions. In order to have a view of the Re value range we work with, we plot Re vs. the channel width, h, in Fig. 8(a) and Re vs. wall wettability ratio in Fig. 8(b). In Fig. 8(a), Re is close to zero for channels around $h < 10\sigma$ and increases thereafter. Fig. 8(b) reveals small Re values past an hydrophilic–wall flow.

3.6. Friction factor

The effect of all flow parameters described before is evaluated on the calculation of the nanoscale Darcy–Weisbach, f (Eq. (6)). In Fig. 9(a), the effect of channel width on Re is incorporated in order to be drawn vs. f in a fully logarithmic plot. It is evident that there exists a linear relation between f and Re, as shown by the linear fit applied. In fact, this diagram could be considered as an extension to a classical Moody diagram, for very low Re (extension to the left). From the diagram, we obtain through a power law fit the following relation.

$$f = 77.19\mathrm{Re}^{-1} \tag{13}$$

Eq. (13) is very close to the classical relation found in the Moody's diagram.

Wall wettability is not a parameter taken into account at the classical theory, but cannot be neglected at the nanoscale. It is of interest to incorporate it in the flow. Fig. 9(b) depicts f vs. Re for channel flows with wall wettability ratios $0.2 < \varepsilon_w/\varepsilon_f < 5.0$.

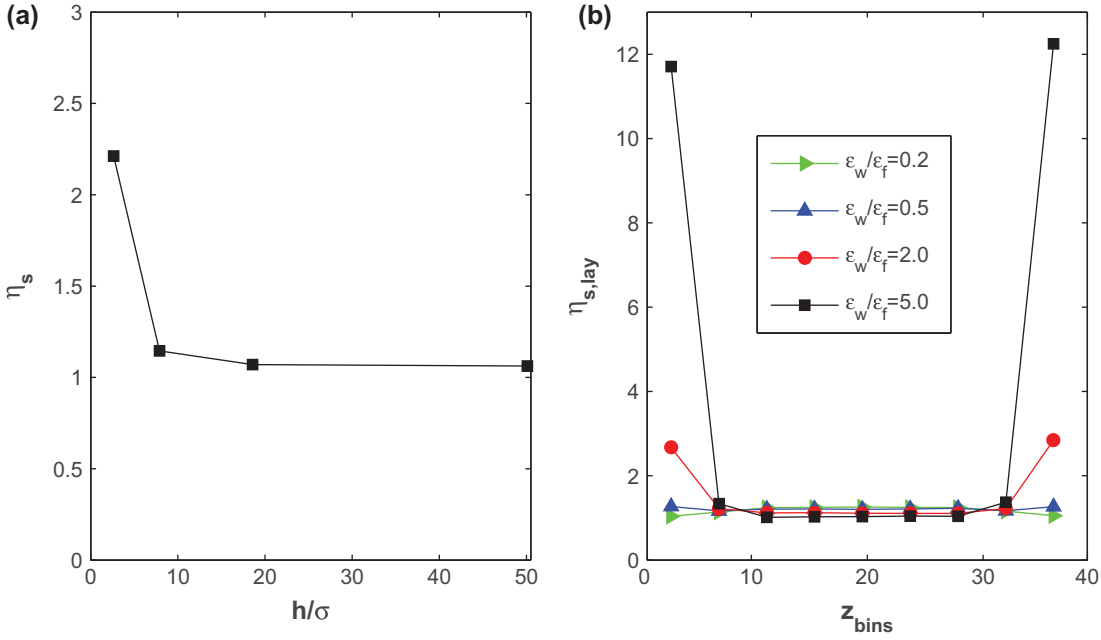

Fig. 7. Shear viscosity values investigated vs. the effect of (a) channel width h, as channel average value and (b) wall wettability ratio, as value in channel layers inside the $h = 18.58\sigma$ channel. Flow conditions are the same as in Fig. 6. Lines are guide to the eye. Values shown in reduced LJ units $\sigma^2/\sqrt{me}$.

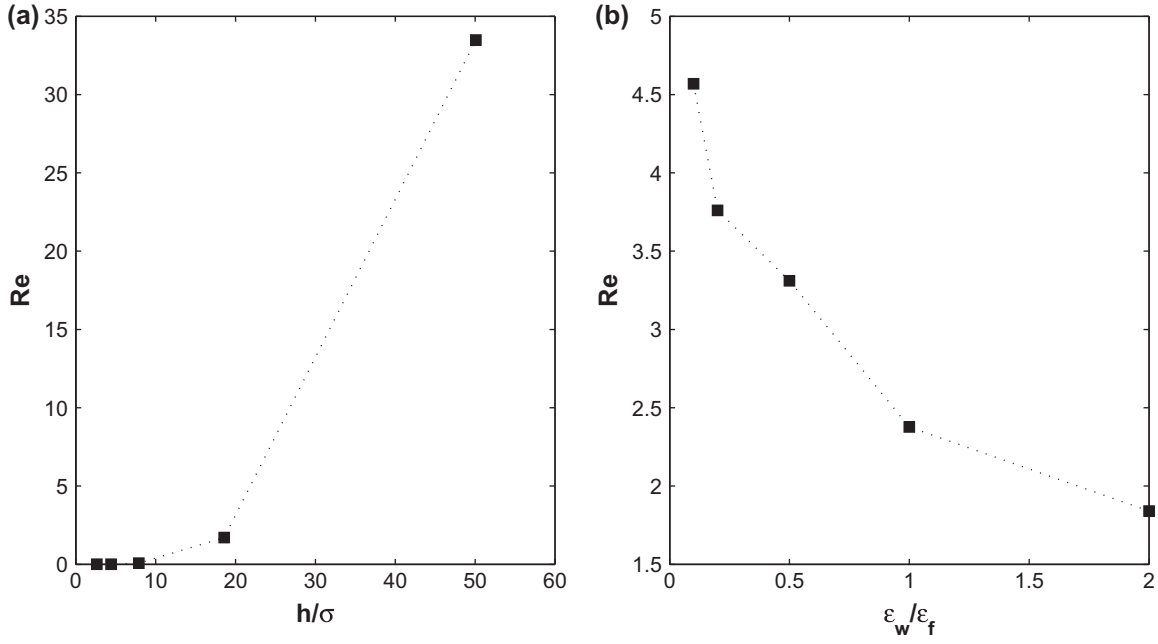

Fig. 8. Re values at the nanoscale shown vs. (a) channel width and (b) wall wettability ratio. Flow conditions are the same as in Fig. 6. Lines are guide to the eye.

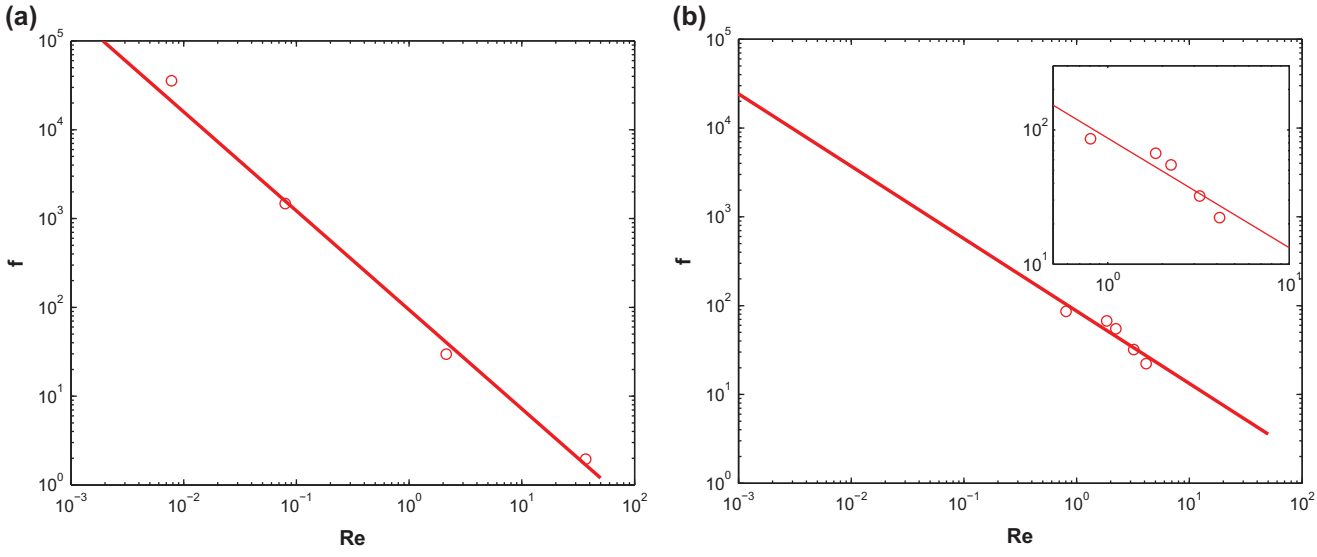

Fig. 9. Fully logarithmic plot of friction factor vs. Re (a) resulting from channel width variation and (b) resulting from wall wettability variation. Lines are linear fits.

The linear fit in Fig. 9(b) gives:

$$f = 86.76\mathrm{Re}^{-0.82} \tag{14}$$

Eq. (14) is still close to the classical prediction of a Moody diagram (within statistical error), and so, wall hydrophobicity/hydrophilicity is a parameter that could be incorporated for Poiseuille-like channel flows.

4. Conclusion

Radial distribution function calculations with molecular dynamics method along various

nanochannels of various widths have been investigated and revealed that the distribution of fluid atoms in the nanochannel is affected by the presence of the walls and the limited width of the nanochannel. This effect seems to be reduced as the nanochannel size increases. It turns out that for nanochannels of height $h > 50\sigma$, the radial distribution function approaches that of the bulk liquid, while for $h < 50\sigma$, differences are noticeable. Wall wettability degree is another significant parameter to be taken into account since it strongly affects fluid behavior near the wall, as an hydrophilic wall attracts fluid atoms, while an hydrophobic wall leads to strong fluid ordering.

The friction factor, as a quantity that applies on macroscale flows, is investigated at the nanoscale and found to be affected by fluid ordering as well as by wall hydrophobicity/hydrophilicity. Our first results show that an extension of the classical Moody's diagram could be constructed, so as to guide applications in small scales, where Re has values around unity. It is evident that such a Moody's extended diagram is to apply on different flow materials (wall and fluid) since there exists different strength of wall/fluid interaction on different materials, which in turn affect wall wettability.

If we combine our MD results with related experiments, this could assist researchers in developing future nanoscale devices. The mechanism of attractive/repelling surfaces shown above could be incorporated to the design of smart surfaces and nanomembranes for water desalination. To further contribute toward this direction, in a future work, it would be interesting to try to connect the behavior observed for a structural property like $g(r)$ and a dynamic property like f to the simulation observation that transport properties (such as the diffusion coefficient, shear viscosity, and thermal conductivity) also vary as a function of the distance from the wall, and how very small variations in structure induce differences in transport properties. If one wishes to investigate the applicability of these findings for water treatment systems, we would note that wall/fluid interaction is the main property that could be incorporated. For example, a nanochannel of height around $h = 10\sigma$ or less, with strongly hydrophobic walls, would present strong fluid ordering near the wall, i.e., increased fluid atom concentration. In case of polluted water flow through a nanochannel, we could expand our findings to keep undesired particles near the solid surface as a means of controlling wall wettability. All these remarks will be employed in a future work.

References

[1] S.J. Kim, S.H. Ko, K.H. Kang, J. Han, Direct seawater desalination by ion concentration polarization, Nat. Nanotechnol. 5 (2010) 297–301.
[2] N. Savage, M.S. Diallo, Nanomaterials and water purification: Opportunities and challenges, J. Nanopart. Res. 7 (2005) 331–342.
[3] A. Noy, H.G. Park, F. Fornasiero, J.K. Holt, C.P. Grigoropoulos, O. Bakajin, Nanofluidics in carbon nanotubes, Nano Today 2(6) (2007) 22–29.
[4] K. Ritos, D. Mattia, F. Calabrò, J.M. Reese, Flow enhancement in nanotubes of different materials and lengths, J. Chem. Phys. 140 (2014) 014702 1–6.
[5] S. Joseph, N.R. Aluru, Why are carbon nanotubes fast transporters of water?, Nano Lett. 8 (2008) 452–458.
[6] R. Das, Md.E. Ali, S. Bee, A. Hamid, S. Ramakrishna, Z.Z. Chowdhury, Carbon nanotube membranes for water purification: A bright future in water desalination, Desalination 336 (2014) 97–109.
[7] P.S. Goh, A.F. Ismail, B.C. Ng, Carbon nanotubes for desalination: Performance evaluation and current hurdles, Desalination 308 (2013) 2–14.
[8] M.P. Allen, T.J. Tildesley, Computer Simulation of Liquids, Clarendon Press, Oxford, 1987.
[9] G. Nagayama, P. Cheng, Effects of interface wettability on microscale flow by molecular dynamics simulation, Int. J. Heat Mass Transfer 47 (2004) 501–512.
[10] F. Sofos, T.E. Karakasidis, A. Liakopoulos, Parameters affecting slip length at the nanoscale, J. Comput. Theor. Nanosci. 10(3) (2013) 1–4.
[11] H.B. Eral, D. van den Ende, F. Mugele, M.H.G. Duits, Influence of confinement by smooth and rough walls on particle dynamics in dense hard-sphere suspensions, Phys. Rev. E 80 (2009) 061403 1–8.
[12] F. Sofos, T.E. Karakasidis, A. Liakopoulos, Transport properties of liquid argon in krypton nanochannels: Anisotropy and non-homogeneity introduced by the solid walls, Int. J. Heat Mass Transfer 52 (2009) 735–743.
[13] A.E. Giannakopoulos, F. Sofos, T.E. Karakasidis, A. Liakopoulos, Unified description of size effects of transport properties of liquids flowing in nanochannels, Int. J. Heat Mass Transfer 55 (2012) 5087–5092.
[14] W. Sparreboom, A. van den Berg, J.C.T. Eijkel, Principles and applications of nanofluidic transport, Nat. Nanotechnol. 4 (2009) 713–720.
[15] S.C. Yang, L.B. Fang, Effect of surface roughness on slip flows in hydrophobic and hydrophilic microchannels by molecular dynamics simulation, Mol. Simul. 31(14–15) (2005) 971–977.
[16] F. Sofos, T.E. Karakasidis, A. Liakopoulos, Surface wettability effects on flow in rough wall nanochannels, Microfluid. Nanofluid. 12 (2012) 25–31.
[17] U. Heinbuch, J. Fischer, Liquid flow in pores: Slip, no-slip, or multilayer sticking, Phys. Rev. A 40 (1989) 1144–1146.
[18] M. Sbragaglia, R. Benzi, L. Biferale, S. Succi, F. Toschi, Surface roughness-hydrophobicity coupling in microchannel and nanochannel flows, Phys. Rev. Lett. 97 (2006) 204503.
[19] F. Sofos, T.E. Karakasidis, A. Liakopoulos, Effects of wall roughness on flow in nanochannels, Phys. Rev. E 79 (2009) 026305.

[20] M. Kalweit, D. Drikakis, Multiscale methods for micro/nano flows and materials, J. Comput. Theor. Nanosci. 5 (2008) 1923–1938.
[21] N. Asproulis, M. Kalweit, D. Drikakis, A hybrid molecular continuum method using point wise coupling, Adv. Eng. Softw. 46(1) (2012) 85–92.
[22] M. Kalweit, D. Drikakis, Coupling strategies for hybrid molecular-continuum simulation methods, Proc. IMechE Part C, J. Mech. Eng. Sci. 222 (2008) 797–806.
[23] N. Aproulis, D. Drikakis, An artificial neural network-based multiscale method for hybrid atomistic-continuum simulations, Microfluid. Nanofluid. 15 (2013) 559–574.
[24] C. Zhang, Y. Chen, Slip behavior of liquid flow in rough nanochannels, Chem. Eng. Process. 85 (2014) 203–208.